SI

An [Fe^{III}$_8$] molecular oxyhydroxide

Daniel J Cutler, Marco Coletta, Mukesh K. Singh, Angelos B. Canaj, Laura J. McCormick, Simon J. Coles, Juergen Schnack and Euan K. Brechin

Synthesis

All manipulations were performed under aerobic conditions, using materials as received. 4-methoxypyridine (CAS RN: 620-08-6, 98.00%, Fluorochem), FeBr$_3$ (CAS RN: 10031-26-2, 98%, Fluorochem), Acetone (99.8%, Merck). Elemental analyses (C, H, N) were performed by The University of Edinburgh, School of GeoSciences microanalysis service.

[Fe^{III}$_8$(μ_3-O)$_6$(μ-OH)$_6$(4-MeOpy)$_{12}$Br$_2$]Br$_4$·(4-MeOpy) (1)

FeBr$_3$ (2 mmol, 0.591 g) was dissolved in 4-methoxypyridine (4-MeOpy, 200 mmol, 20 ml). The resulting dark orange solution was stirred at room temperature for 2.5 hours, before being filtered. Vapour diffusion of acetone into the filtrate resulted in plate-shaped orange crystals suitable for single crystal X-ray diffraction. Yield: ≤ 10%. Elemental analysis: C, 36.84 (36.65); H, 3.84 (4.15); N, 7.16 (7.17).

Single Crystal and Powder X-ray diffraction

A suitable crystal with dimensions 0.12 × 0.06 × 0.02 mm^3 was selected and mounted on a MITIGEN holder in perfluoroether oil on a Rigaku FRE+ equipped with VHF Varimax confocal mirrors and an AFC12 goniometer and HyPix 6000 detector. The crystal was kept at a steady T = 100(2) K during data collection. The structure was solved with the ShelXT 2018/2 structure solution program using the dual methods solution method and by using Olex2 1.3 as the graphical interface. The model was refined with version 2018/3 of ShelXL 2018/3 (Sheldrick, 2015) using full matrix least squares minimisation on F^2 minimisation.[1,2] Powder XRD measurements were collected on freshly prepared samples of **1** using a Bruker D2 PHASER with nickel filtered Cu radiation at power 30 kW and current 10mA. Diffraction patterns are measured from 2θ = 5° - 30°; step size, 0.0101°.
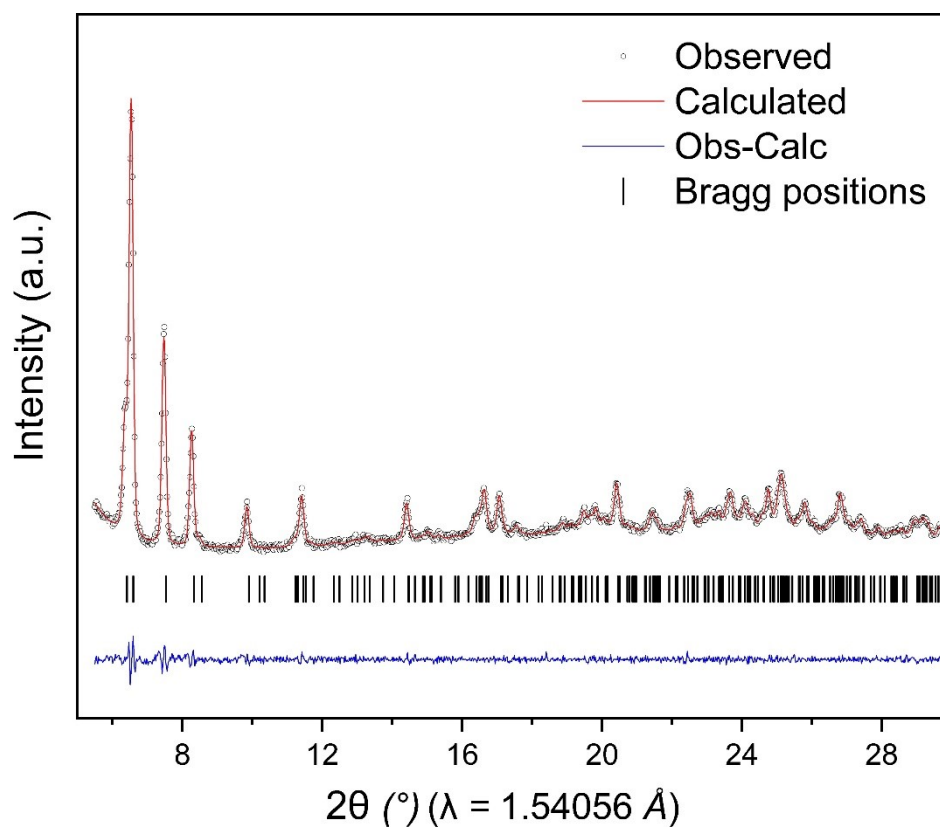
Thermogravimetric Analysis

TGA analysis was performed on a Netzsch STA 449F1 instrument with a platinum furnace under a nitrogen atmosphere (20 ml min^{-1}) in the 20 – 900 K temperature range (2 K min^{-1}).

Magnetic Measurements

Variable-temperature, solid-state direct current (dc) magnetic susceptibility data down to 2.0 K were collected on a Quantum Design MPMS-XL SQUID magnetometer equipped with a 7 T DC magnet. The crystalline sample was embedded in eicosane and diamagnetic corrections were applied to the observed paramagnetic susceptibilities.

**Table S1:** Crystallographic details for compound **1**.

| Compound	1
Formula	$C_{84}H_{109}Br_6Fe_8N_{14}O_{28.5}$
$D_{calc.}$/ g cm^{-3}	1.717
μ/mm^{-1}	3.457
Formula Weight	2697.11
Colour	orange
Shape	plate-shaped
Size/mm^3	0.12×0.06×0.02
T/K	100(2)
Crystal System	monoclinic
Space Group	$C2/c$
a/Å	24.5496(9)
b/Å	27.2170(10)
c/Å	16.4374(7)
α/°	90
β/°	108.242(4)
γ/°	90
V/Å^3	10430.9(7)
Z	4
Z'	0.5
Wavelength/Å	0.71073
Radiation type	Mo K$_\alpha$
Θ_{min}/°	1.496
Θ_{max}/°	27.101
Measured Refl's.	80637
Indep't Refl's	11498
Refl's I≥2 σ(I)	8514
R_{int}	0.1172
Parameters	736
Restraints	26
Largest Peak	1.057
Deepest Hole	-0.692
GooF	1.018
wR_2 (all data)	0.1148
wR_2	0.1044
R_1 (all data)	0.0732
R_1	0.0456
CCDC	2163355

Figure S1. Refinement of the experimental diffraction data of **1** collected at room temperature by using the Le Bail method and the single-crystal structural model as starting parameters. Experimental (black circles), calculated (red line), difference plot [(I_{obs}–I_{calc})] (blue line) and Bragg positions (black ticks). Monoclinic, *C*2/*c*; *a* = 24.6136 Å; *b* = 27.5062 Å; *c* = 16.4066 Å; α = γ = 90°; β = 107.6354 °; R_{exp} = 1.16 %, R_{wp} = 1.72 %, GoF = 1.48.
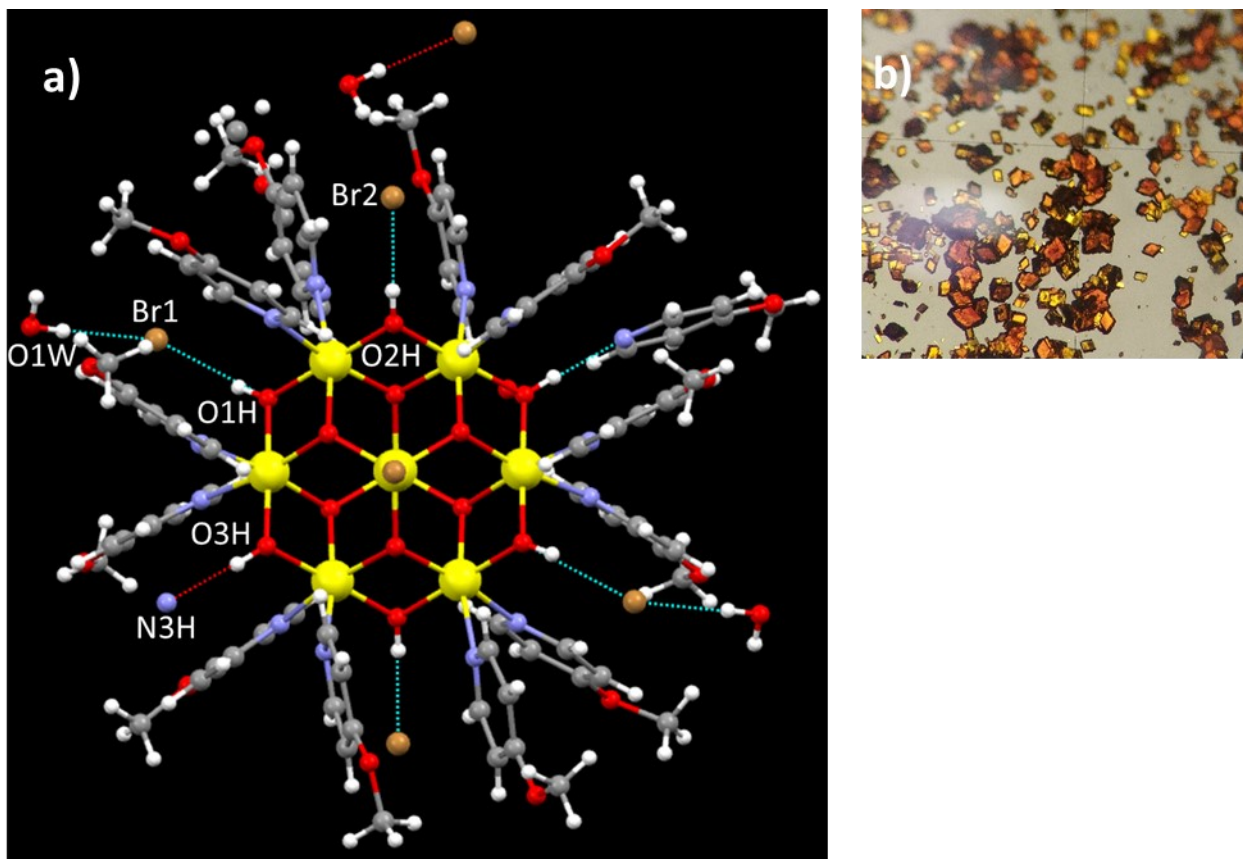
Figure S2. a) H-bonding interactions between the cluster cation of **1**, the Br counter anions and H_2O, Me-OPy molecules of crystallisation. H-bonds are shown as dashed blue lines. Colour code: Fe = yellow, O = red, C = grey, N = blue, H = white, Br = brown. b) Microscope image of the crystals of **1**.
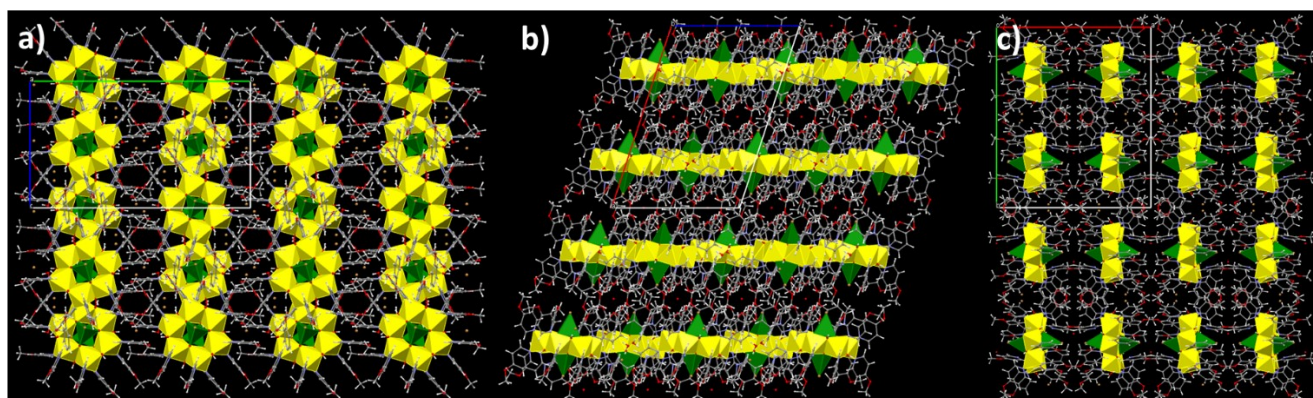
Figure S3. Packing diagram of **1** viewed down the three unit cell axes, respectively, highlighting the layered packing of the cluster cations in the extended structure. The Fe^{III} ions are shown in polyhedral format with octahedral ions in yellow and tetrahedral ions in green.
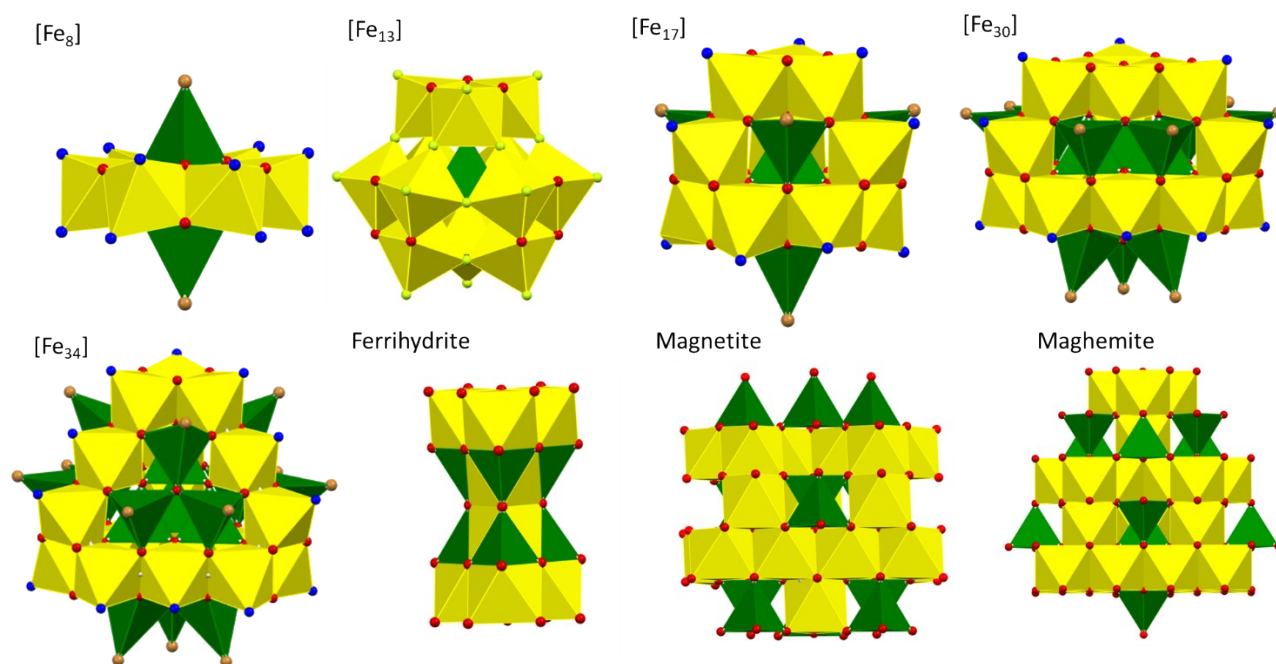
Figure S4. A structural comparison of the structures of [Fe$_8$], [Fe$_{13}$], [Fe$_{17}$], [Fe$_{30}$], [Fe$_{34}$], magnetite, maghemite and ferrihydrite.
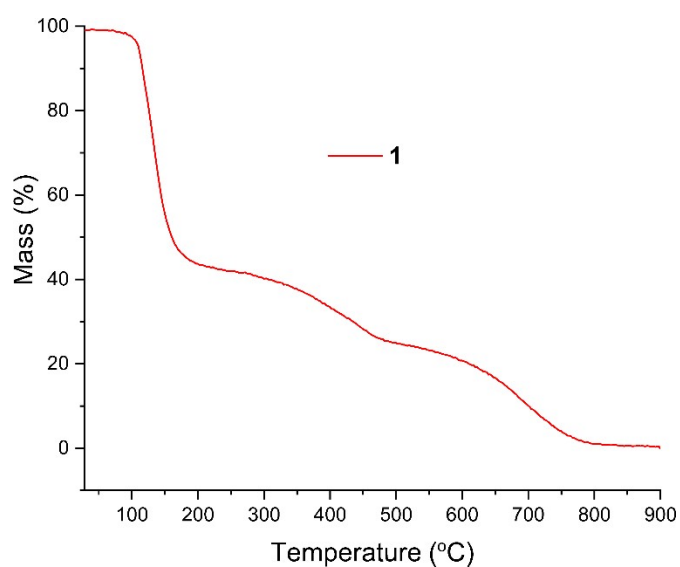

Figure S5. Thermogravimetric analysis of **1** (red line) under a nitrogen flow of 20 ml min^{-1} and heating rate 2 °C min^{-1}. The weight loss of 39 % below 111 °C corresponds to the loss of ten 4-methoxypyridine molecules.

Computational Details

For the DFT calculations we have used the Gaussian 09 suite[3] of programs to estimate the magnetic exchange coupling constants J_{ring} and J_{cap} (where J_{ring} is the interaction between Fe_{oct}-Fe_{oct} and J_{cap} is the interaction between Fe_{oct}-Fe_{tet}) using two sets of calculations. For the first set of calculations, we have used pairwise exchange interaction calculations keeping only the two paramagnetic centres of interest, and replacing the remaining six paramagnetic ions with Ga^{III} ions (Models **1A** and **1B**). For the second set of calculations, we have kept two adjacent Fe_{Oct} centres and one Fe_{tet} centre, replacing the remaining five Fe^{III} ions with five diamagnetic Ga^{III} ions (Model **1C**). For **1C**, we have calculated one high spin configuration with all three Fe^{III} spins up ($S = 15/2$) and three broken symmetry configurations with one of the Fe^{III} centres spin down ($S = 5/2$). We have employed the hybrid B3LYP functional,[4] along with the TZV basis set for Fe, the SVP basis set for Ga, O, N, and the SV basis set for C and H.[5] Density Functional Theory (DFT), together with Noodleman's broken symmetry[6] approach, is established as a reliable methodology for estimating exchange interactions with high accuracy.[7] Overlap integral calculations between non-orthogonal singly occupied molecular orbitals of Fe^{III} centres have been performed to analyse the sign and magnitude of magnetic exchange parameter.[7]

(a)

(b)

(c)
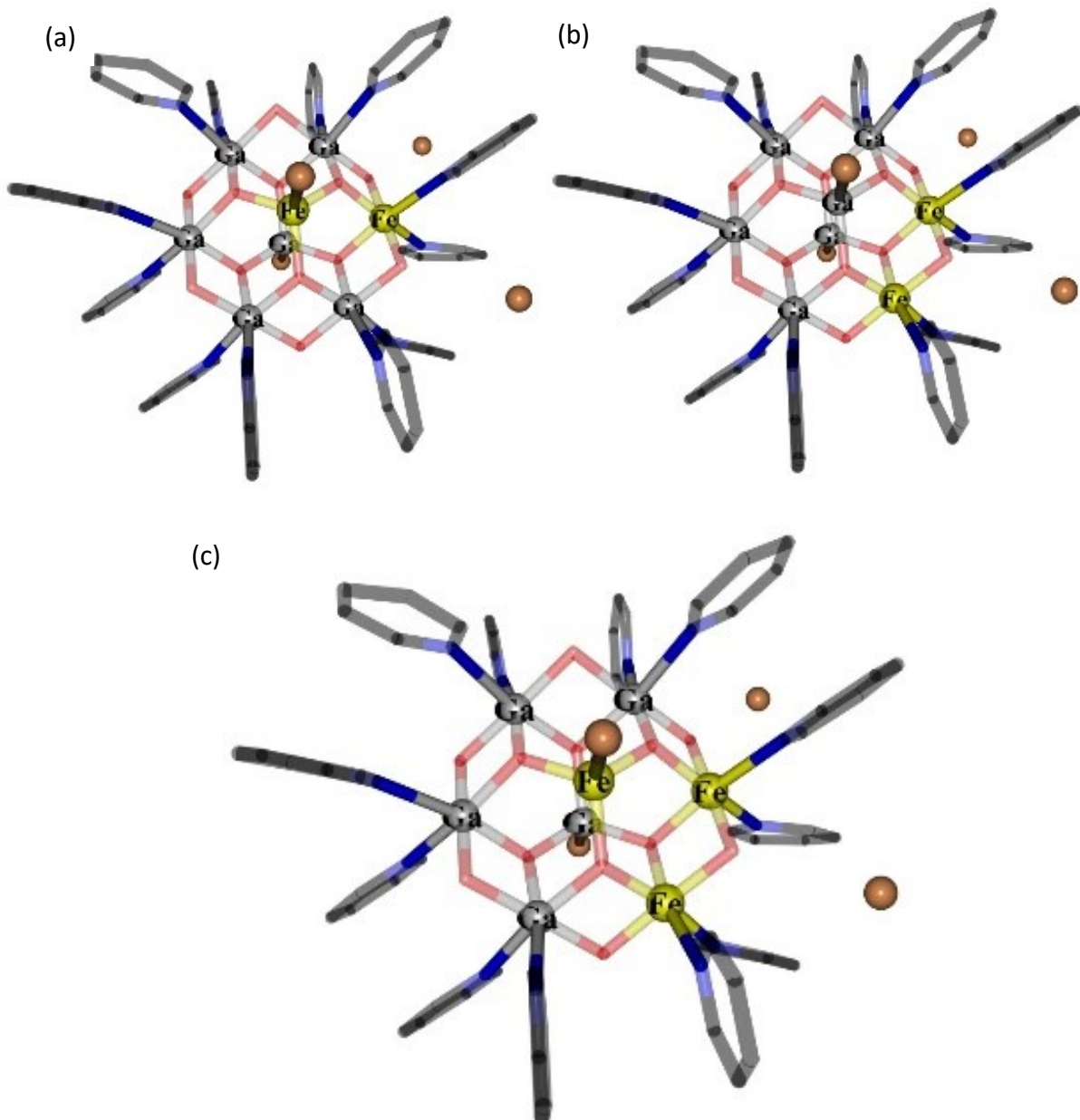
Figure S6. Dimeric models **1A** (a) and **1B** (b), and trimeric model **1C** (c) used for estimating J_{ring} (Fe_{oct}-Fe_{oct}) and J_{cap} (Fe_{oct}-Fe_{tet}).
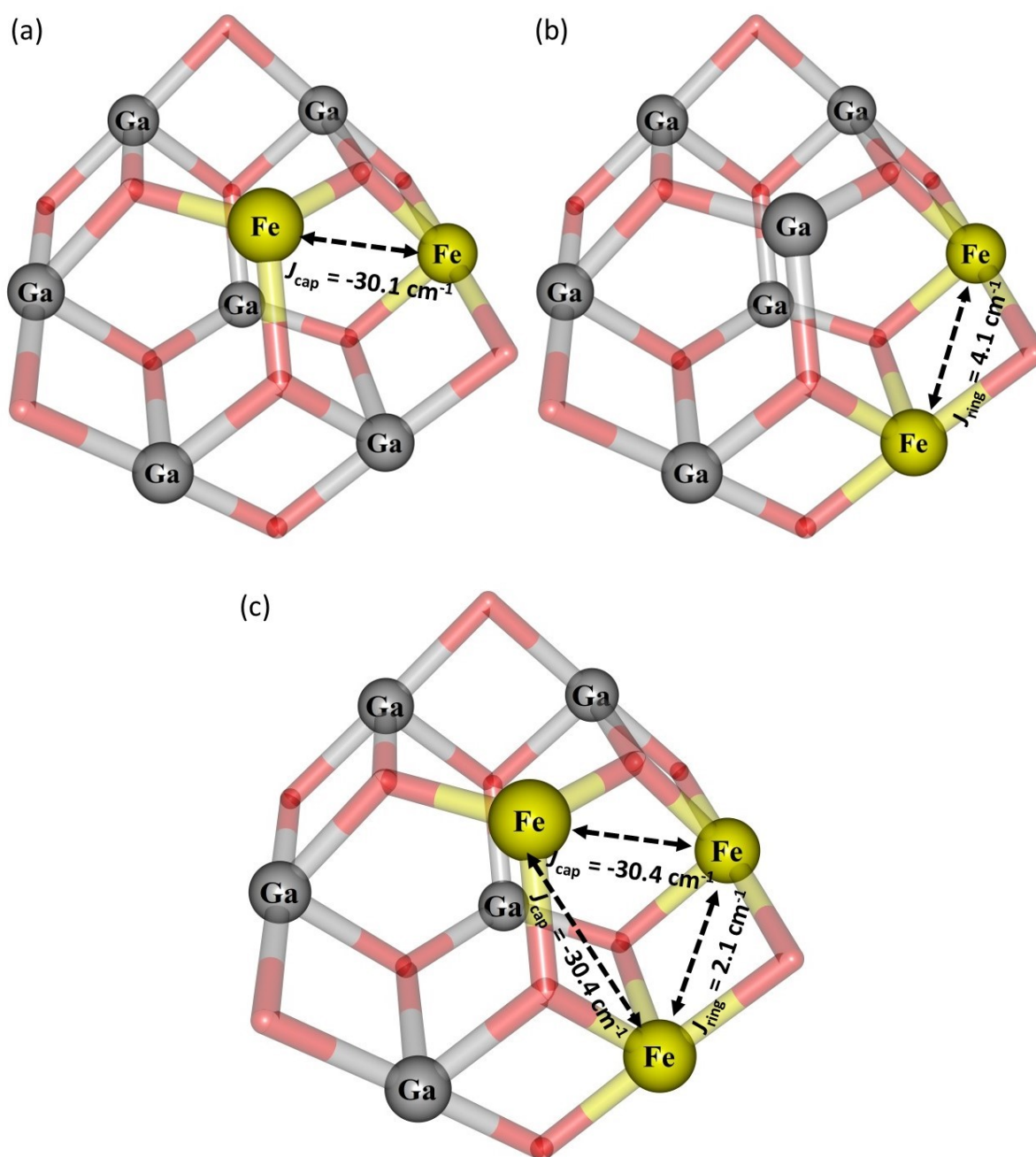
Figure S7. DFT estimated J_{ring} (Fe$_{Oct}$-Fe$_{Oct}$) and J_{cap} (Fe$_{Oct}$-Fe$_{Tetr}$) magnetic exchange interactions employing the dimeric models **1A** (a) and **1B** (b), and the trimeric model **1C** (c). Note that for model **1C** the errors found for both exchange interactions are less than 0.1.

Table S2. DFT estimated overlap integrals for the dimeric models **1A** and **1B** used to calculate J_{ring} (Fe$_{oct}$-Fe$_{oct}$) and J_{cap} (Fe$_{oct}$-Fe$_{tet}$). The red value indicates strong magnetic orbital overlap, whereas the green values suggest moderate magnetic orbital overlaps. Black numbers represent orthogonal/weak magnetic orbital overlaps. Note that stronger antiferromagnetic exchange interactions are observed between paramagnetic centres with a larger number of strong or moderate overlap integrals, and vice versa.

J_{ring}	Fe$_{oct}(\alpha)$	d_{yz}	d_{xy}	d_{xz}	$d_{x^2-y^2}$	d_{z^2}
Fe$_{oct}(\beta)$	d_{yz}	0.055	0.017	0.011	0.070	0.008
	d_{xy}	0.028	0.021	0.030	0.040	0.041
	d_{xz}	0.028	0.036	0.040	0.056	0.030
	$d_{x^2-y^2}$	0.007	0.035	0.047	0.014	0.015
	d_{z^2}	0.008	0.001	0.013	0.015	0.001

J_{cap}	Fe$_{tet}(\alpha)$	d_{yz}	d_{xz}	d_{z^2}	d_{xy}	$d_{x^2-y^2}$
Fe$_{oct}(\beta)$	d_{yz}	0.079	0.064	0.054	0.023	0.034
	d_{xy}	0.048	0.087	0.000	0.093	0.070
	d_{xz}	0.056	0.006	0.047	0.010	0.006
	$d_{x^2-y^2}$	0.045	0.001	0.066	0.056	0.099
	d_{z^2}	0.004	0.013	0.023	0.042	0.050

(a)

$<\text{Fe}(\alpha)d_{yz}|p_{x/y/z}|\text{Fe}(\beta)d_{yz}> = 0.055$

(b)

$<\text{Fe}(\alpha)d_{x^2-y^2}|p_{x/y/z}|\text{Fe}(\beta)d_{yz}> = 0.070$

(c)

$<\text{Fe}(\alpha)d_{x^2-y^2}|p_{x/y/z}|\text{Fe}(\beta)d_{xz}> = 0.056$

(d)

$<\text{Fe}(\alpha)d_{yz}|p_{x/y/z}|\text{Fe}(\beta)d_{yz}> = 0.079$

(e)

$<\text{Fe}(\alpha)d_{yz}|p_{x/y/z}|\text{Fe}(\beta)d_{xz}> = 0.056$

(f)

$<\text{Fe}(\alpha)d_{xz}|p_{x/y/z}|\text{Fe}(\beta)d_{yz}> = 0.064$

(g)

$<\text{Fe}(\alpha)d_{xz}|p_{x/y/z}|\text{Fe}(\beta)d_{xy}> = 0.087$

(h)

$<\text{Fe}(\alpha)d_{z^2}|p_{x/y/z}|\text{Fe}(\beta)d_{yz}> = 0.054$

(i)

$<\text{Fe}(\alpha)d_{z^2}|p_{x/y/z}|\text{Fe}(\beta)d_{x^2-y^2}> = 0.066$

(j)

$<\text{Fe}(\alpha)d_{xy}|p_{x/y/z}|\text{Fe}(\beta)d_{xy}> = 0.093$

(k)

$<\text{Fe}(\alpha)d_{xy}|p_{x/y/z}|\text{Fe}(\beta)d_{x^2-y^2}> = 0.056$

(l)

$<\text{Fe}(\alpha)d_{x^2-y^2}|p_{x/y/z}|\text{Fe}(\beta)d_{xy}> = 0.070$

SI

$$\langle Fe(\alpha)d_{x^2-y^2}|p_{x/y/z}|Fe(\beta)d_{x^2-y^2}\rangle = 0.070$$

$$\langle Fe(\alpha)d_{x^2-y^2}|p_{x/y/z}|Fe(\beta)d_{z^2}\rangle = 0.050$$
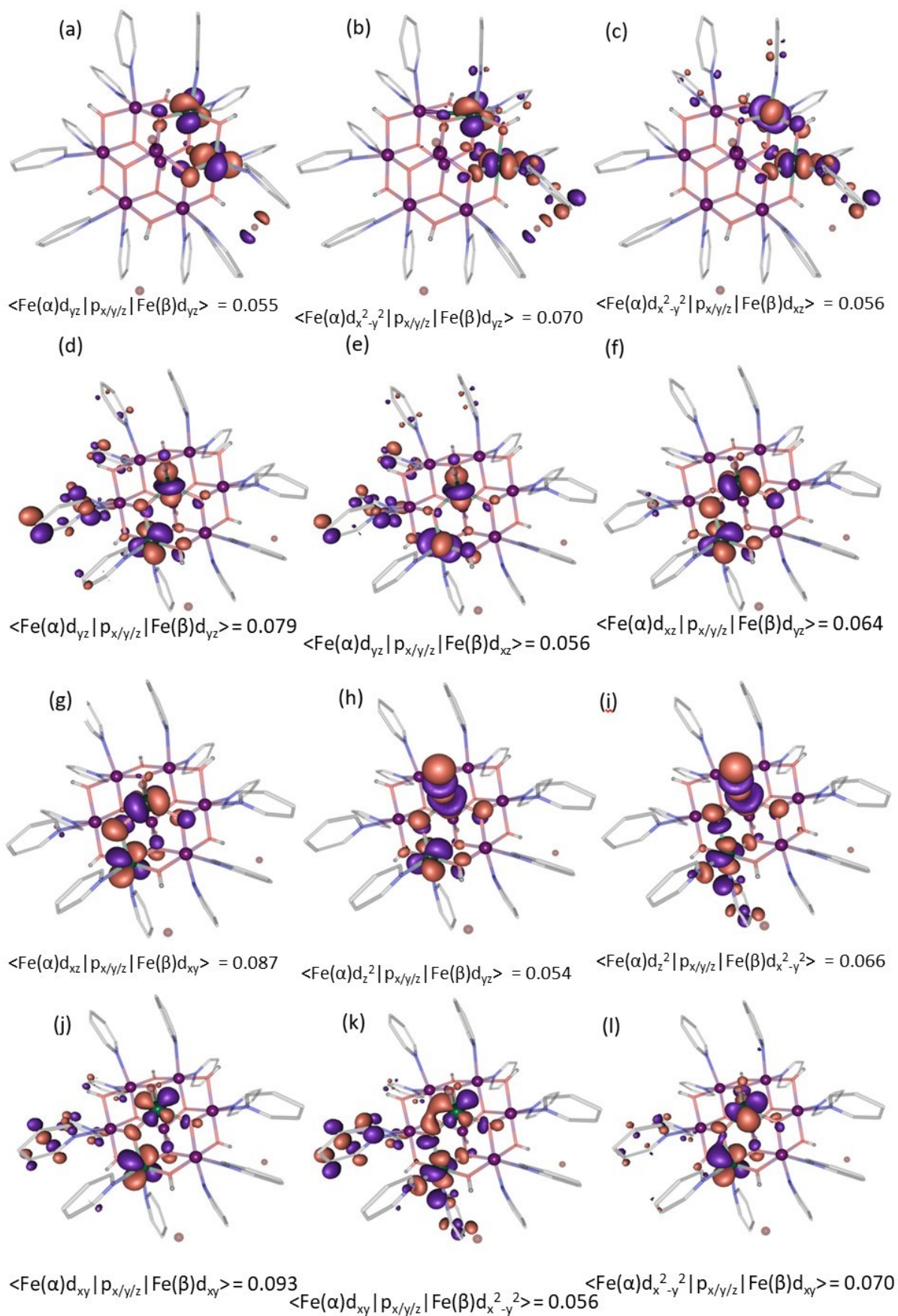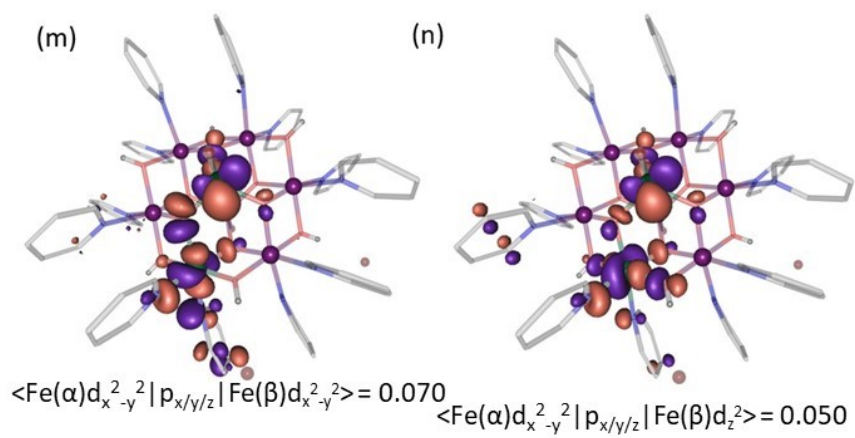
Figure 8. Representative overlap integrals showing strong and moderate Fe^{III} based SOMO(s)-SOMO(s) overlap interactions for J_{ring} (Fe_{oct}-Feo_{ct}) (**a-c**) and J_{cap} (Fe_{Oct}-Fe_{Tetr}) (**d-n**).
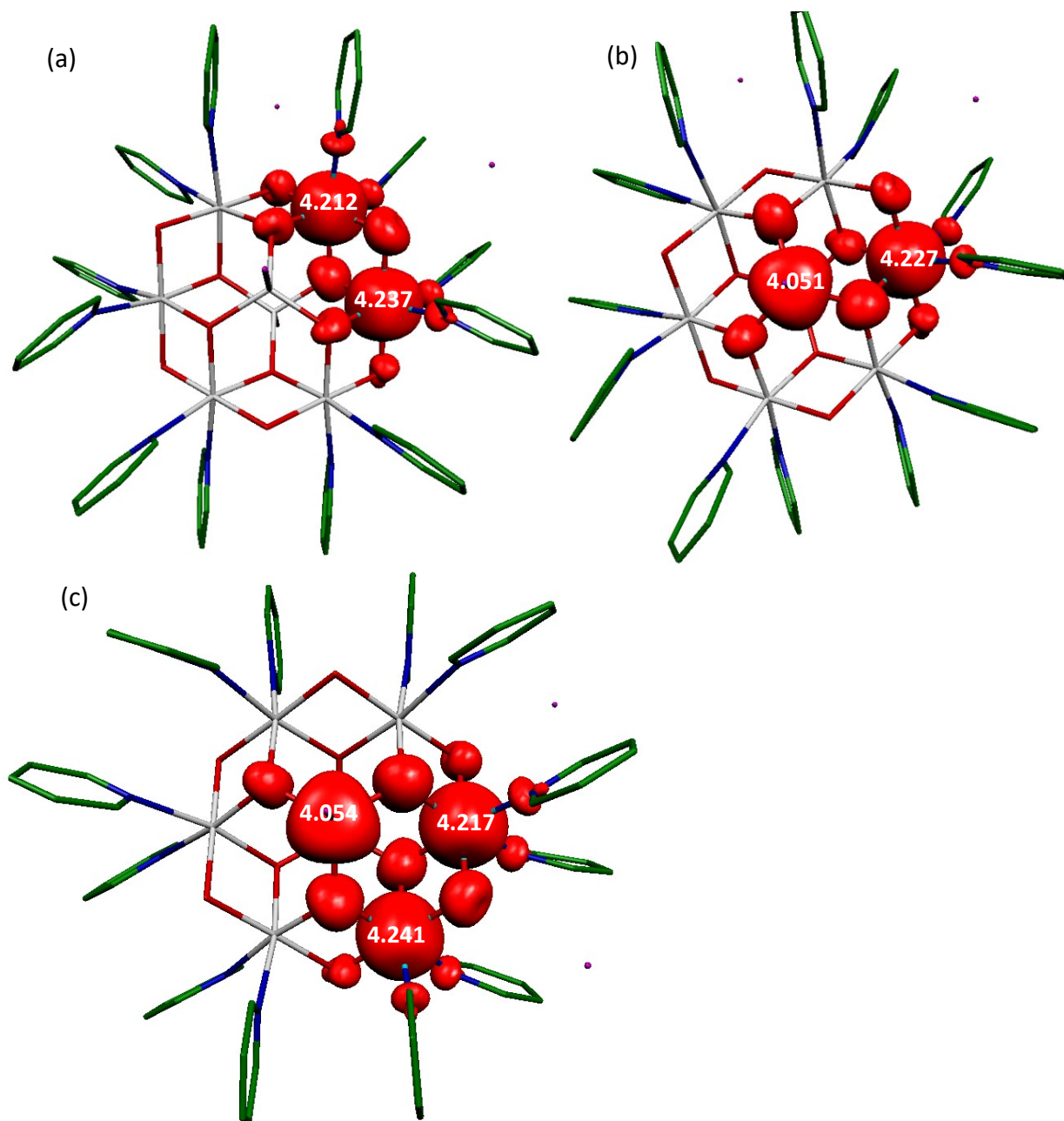
Figure 9. DFT computed spin density plots for models **1A** (a)**, 1B** (b) and **1C** (c). The iso-density surfaces shown corresponds to a value of 0.01 e$^-$/bohr^3. The spin density plots indicate a strong spin delocalization mechanism, with spin density values on the Fe^{III} ions between 4.051 - 4.241. The largest spin density is detected on μ_3-O atoms.

References

1. G. M. Sheldrick, *Acta Crystallogr. Sect. C: Cryst. Struct. Commun.,* 2015, **71**, 3-8.

2. O. V. Dolomanov, L. J. Bourhis, R. J. Gildea, J. A. K. Howard and H. Puschmann, *J. Appl. Crystallogr.,* 2009, **42**, 339-341.

3. M. J. Frisch, G. W. Trucks, H. B. Schlegel, G. E. Scuseria, M. A. Robb, J. R. Cheeseman, G. Scalmani, V. Barone, B. Mennucci, G. A. Petersson, H. Nakatsuji, M. Caricato, X. Li, H. P. Hratchian, A. F. Izmaylov, J. Bloino, G. Zheng, J. L. Sonnenberg, M. Hada, M. Ehara, K. Toyota, R. Fukuda, J. Hasegawa, M. Ishida, T. Nakajima, Y. Honda, O. Kitao, H. Nakai, T. Vreven, J. A. Montgomery, Jr., J. E. Peralta, F. Ogliaro, M. Bearpark, J. J. Heyd, E. Brothers, K. N. Kudin, V. N. Staroverov, T. Keith, R. Kobayashi, J. Normand, K. Raghavachari, A. Rendell, J. C. Burant, S. S. Iyengar, J. Tomasi, M. Cossi, N. Rega, J. M. Millam, M. Klene, J. E. Knox, J. B. Cross, V. Bakken, C. Adamo, J. Jaramillo, R. Gomperts, R. E. Stratmann, O. Yazyev, A. J. Austin, R. Cammi, C. Pomelli, J. W. Ochterski, R. L. Martin, K. Morokuma, V. G. Zakrzewski, G. A. Voth, P. Salvador, J. J. Dannenberg, S. Dapprich, A. D. Daniels, O. Farkas, J. B. Foresman, J. V. Ortiz, J. Cioslowski, and D. J. Fox, Gaussian 09, Revision E.01, Wallingford CT, 2013.

4. a) A. D. Becke, *Phys. Rev. A* 1988, *38*, 3098-3101; b) A. D. Becke, *J. Chem. Phys.,* 1993, **98**, 5648; c) C. Lee, W. Yang, R. G. Parr, *Phys. Rev. B,* 1988, **37**, 785.

5. a) A. Schäfer, H. Horn, R. Ahlrichs, *J. Chem. Phys.,* 1992, **97**, 2571-2577; b) A. Schäfer, C. Huber, R. Ahlrichs, *J. Chem. Phys.,* 1994, **100**, 5829; c) G. E. Scuseria, H. F. Schäfer, *J. Chem. Phys.,* 1989, **90**, 3700.

6. L. Noodleman, *J. Chem. Phys,.* 1981, **74**, 5737.

7. a) M. K. Singh, *Dalton Trans.,* 2020, **49**, 4539-4548; b) M. K. Singh, G. Rajaraman, *Inorg. Chem.,* 2019, **58**, 3175-3188; c) M. K. Singh, G. Rajaraman, *Chem. Eur. J.,* 2015, **21**, 980-983; d) J. Caballero-Jiménez, F. Habib, D. Ramírez-Rosales, R. Grande-Aztatzi, G. Merino, I. Korobkov, M. K. Singh, G. Rajaraman, Y. Reyes-Ortega, M. Murugesu, *Dalton Trans.,* 2015, **44**, 8649; e) C. McDonald, S. Sanz, E. K. Brechin, M. K. Singh, G. Rajaraman, D. Gaynor, L. F. Jones, *RSC Adv.,* 2014, **4**, 38182. f) A. E. Dearle, D. J. Cutler, H. W. L. Fraser, S. Sanz, E. Lee, S. Dey, I. F. Diaz-Ortega, G. S. Nichol, H. Nojiri, M. Evangelisti, G. Rajaraman, J. Schnack, L. Cronin, E. K. Brechin, *Angew. Chem. Int. Ed.,* 2019, **58**, 16903-16906; g) M. Coletta, T. G. Tziotzi, M. Gray, G. S. Nichol, M. K. Singh, C. J. Milios, E. K. Brechin, *Chem. Commun.,* 2021, **57**, 4122-4125; h) D. J. Cutler, M. K. Singh, G. S. Nichol, M. Evangelisti, J. Schnack, L. Cronin, E. K. Brechin, *Chem. Commun.,* 2021, **57**, 8925-8928.